Rotor Performance Predictions for UAM - Single vs Coaxial Rigid Rotors

Jason Cornelius
Doctoral Student
Department of Aerospace Engineering
The Pennsylvania State University
University Park, PA 16802

Sven Schmitz
Associate Professor
Department of Aerospace Engineering
The Pennsylvania State University
University Park, PA 16802

ABSTRACT

The recent increased interest in advanced air mobility (AAM), specifically within urban air mobility (UAM) and electric vertical take-off and landing (eVTOL) applications, has created a need to better understand and be able to predict the performance of these vehicles. Various configurations of AAM platforms are constantly being proposed, but the majority of them are based on a multi-rotor system consisting of single or coaxial rotors. This work summarizes a CFD model development using a hybrid BEMT and unsteady RANS flow solver, Rotorcraft CFD, which predicts rotor performance at a fidelity suitable for engineering design in a fraction of the time required by conventional CFD methods. Single and coaxial rotor configurations are presented using two-bladed KDE 30.5" rotors and are compared to test data obtained in the NASA Langley 14- by 22- ft. Subsonic Tunnel Facility. The simulations were run with both fully-turbulent and free-transition airfoil performance tables to quantify the associated uncertainty. Simulation results comparing an isolated single rotor to a coaxial rotor system are also presented.

NOTATION

A	Rotor Disk Area [m^2]
AAM	Advanced Air Mobility
BEMT	Blade Element Momentum Theory
CAD	Computer Aided Design
CFD	Computational Fluid Dynamics
CPU	Central Processing Unit
C_T	Thrust Coefficient = T/(ρAΩ^2 R^2)
C_Q	Torque Coefficient = Q/(ρAΩ^2 R^3)
D	Rotor Diameter [m]
eVTOL	Electric Vertical Take-Off and Landing
GPU	Graphics Processing Unit
NACA	National Advisory Committee for Aeronautics
P	Rotor Power [W]
PAV	Planetary Aerial Vehicle
PWM	Pulse Width Modulation
Torque, Q	Rotor Torque [N-m]
R	Rotor Blade Radius [m]
r	Radial Location [m]
RANS	Reynolds-averaged Navier-Stokes
RotCFD	Rotorcraft Computational Fluid Dynamics
RPM	Revolutions per Minute
SA	Shaft Angle, [deg]
Thrust, T	Rotor Thrust [N]
TWS	Turbulent Wake State
VRS	Vortex Ring State
UAM	Urban Air Mobility
WBS	Windmill Brake State
ρ	Density [kg/m^3]

INTRODUCTION

Coaxial rotor systems are finding increased use and interest from several different sectors of the rotorcraft market due to their condensed packaging, higher redundancy in multi-rotor systems, and benefits in enabling high-speed forward flight. Whether it be full-sized helicopters such as the Sikorsky XH-59A, X2, or the S-97 [Refs. 1-3], new light helicopter designs and UAM applications for commercial transportation [Refs. 4-7], or smaller unmanned systems that fly both here on Earth and explore other worlds, Refs. [8-9], this configuration is continually seeing more use. The increasing demand for coaxial rotors comes along with an increasing need to understand how they operate to improve their efficiency and performance. A large set of conceptual, computational, and wind-tunnel based studies have been conducted to increase the knowledge base for these systems; for example, early work done by Gessow, Harrington, and Dingeldein at the NASA Langley Research Center, Refs. [10-12], studied the effects of planform design and rotor-rotor interactions on rotor efficiency. Coleman later summarized both the theoretical and experimental research to date on these rotor systems, Ref. [13]. In addition to Coleman's work, Ramasamy further summarized hover data for coaxial rotors to more closely study the interference effects, Ref. [14]. More recently, Yeo summarized design approaches and predictive

Presented at the Vertical Flight Society's Aeromechanics for Advanced Vertical Flight Technical Meeting, January 25-27, 2022.

capabilities of coaxial and compound helicopter configurations, Ref. [15].

The analyses presented throughout this work focus on a growing subset of fixed-pitch coaxial rotor systems, i.e. small-scale (less than 2 m diameter), stiff (1st flap frequency > 1.5/Rev), RPM-controlled (variable speed), and with large rotor separation (spacing > D/5). This blade stiffness is higher, and rotor spacing larger, than typically analyzed for conventional helicopter design and can be representative of some eVTOL and UAM configurations. Much work has been carried out by Silva and Johnson, Refs. [16-20], to develop NASA reference vehicles to aid the recent increase in interest for developing these types of vehicles. Some of the NASA reference vehicles have designs more similar to conventional rotorcraft, but a few of the reference vehicles are similar to the configurations discussed in this work. Some previous studies have also focused on characterizing the rotor aerodynamic performance, rotor acoustic signatures, and rotor dynamics of these configurations, Refs. [6, 7, 8, 9, 21-23]. New studies delving further into the analysis of these vehicles range topics covering comprehensive and CFD analyses, handling qualities, system design, hazard analysis, and wind-tunnel testing, Refs. [24-33]. Of particular interest to this work are recent studies in mid-air deployment and high rates of descent with these vehicles, Refs. [34-38]. One recent study also analyzed rotor phase control of multi-rotor configurations to reduce vibratory loading, Ref. [39]. It was found that controlling the individual rotor phase angles can be very effective at cancelling out, or at least reducing, vibratory loads at the aircraft center. Another recent study proposed methods to minimize vibratory loading of these vehicles, Ref. [40].

These multi-rotor systems are also being used for space exploration of other celestial bodies such as Mars and Titan. The successful flight of the Mars Ingenuity Helicopter in April 2021 marked the first flight of a heavier-than-air vehicle on another planet, Refs. [41-44]. Currently, the Dragonfly lander is planned to be the second helicopter sent into space following in Ingenuity's footsteps. These types of planetary aerial vehicles (PAVs) have been proposed several times over the previous two decades for scientific missions and exploration of various planetary bodies in our Solar System, Refs. [45-53]. Following the success of Ingenuity and the awarding of the NASA New Frontiers funding to Dragonfly, a surge of renewed interest has developed around the capabilities these vehicles bring to planetary science and exploration, Refs. [54-59].

The majority of these PAVs are based on distributed electric propulsion in multi-rotor configurations. This setup is very much in line with the previously discussed eVTOL and UAM movements. Thus, several applications, all based on a similar configuration, are drawing much attention and funding into the rotorcraft research community. This work will focus on the aerodynamic modeling and rotor performance prediction of a particular single and coaxial rotor configuration.

MOTIVATION AND OBJECTIVES

Efforts have been underway to develop and verify a coaxial rotor CFD model to predict rotor performance throughout various flight conditions and rotor flow states. Wind tunnel tests were conducted at the NASA Langley 14- by 22- ft. Subsonic Tunnel Facility to generate a set of experimental coaxial and single rotor performance data for the type of configuration previously mentioned, i.e. a small-scale, stiff, fixed-pitch, RPM-controlled, coaxial rotor with large inter-rotor spacing. The major developments of the CFD modeling approach for analyzing both single and coaxial rotors over a wide range of flight conditions are summarized. Recent studies quantifying airfoil performance table uncertainty are also presented. These efforts aim to document the progress to date and identify opportunities to further improve the modeling approach and methodology moving forward.

The objectives of this work are to:

1. Summarize major developments in an efficient CFD model for multi-rotor performance prediction.
2. Document the effects of using fully-turbulent (forced transition) versus free-transition airfoil tables on CFD rotor performance predictions.
3. Compare single versus coaxial rotor performance across a wide range of flight conditions.

WIND TUNNEL TEST SETUP

The experimental test setup of the coaxial rotor test stand is shown in the NASA Langley 14- by 22- ft. Subsonic Tunnel Facility in Figure 1 along with a schematic of the test stand in Figure 2, Ref. [60]. The motors and rotors are commercial off the shelf products and were procured from KDE, Ref. [61]. The method to control the rotors with a pulse width modulation (PWM) signal is referred to as throttle control, which is reported by KDE on a percent scale from 0% to 100%. Each throttle position roughly corresponds to a specific RPM, but the resulting RPM can be slightly different based on a given wind-tunnel test condition and the instantaneous torque on the motors. The throttle settings used in the wind-tunnel test were 25, 50, 75, and 90%, which loosely correspond to about 1600, 2880, 3900, and 4515 RPM depending on the rotor shaft angle. ATI load cells, Ref. [62], placed below each motor were used to record the three forces and three moments for each rotor versus time. Relevant parameters defining the basic coaxial rotor setup and operational conditions are included in Table 1.

Table 1. Coaxial Rotor System Parameters

Variable, units (if applicable)	Value
Diameter (D), in	30.5
Inter-rotor Spacing, in	D/3
RPM Range	~1600-4515
Cut-out Radius	0.117 r/R
Reynolds # Range at 25% R	65k – 180k
Mach # Range at 25% R	0.05 – 0.13
Reynolds # Range at 75% R	162k – 441k
Mach # Range at 75% R	0.15 – 0.40

One of the objectives of this work is to give a brief overview of the modeling advancements learned over the past two years. For a much more thorough description of the wind-tunnel test, the CFD model development, and the verification and uncertainty quantification procedures, however, the authors suggest the recently submitted manuscript, Ref. [60].

Figure 1. Rotor Stand in NASA Langley 14- by 22-ft. Subsonic Tunnel Facility, Ref. [60].

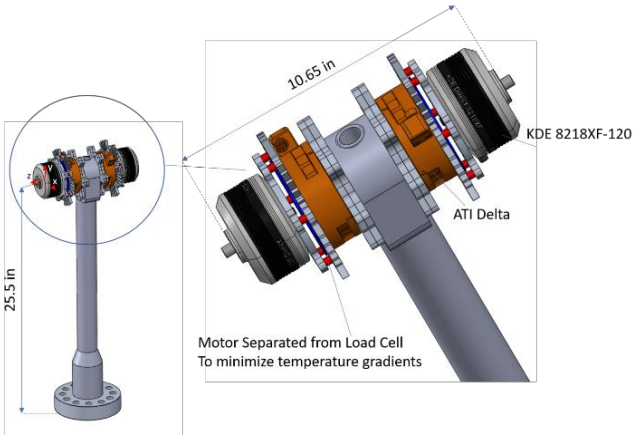

Figure 2. KDE 30.5" Coaxial Rotor Schematic, Ref. [60].

COMPUTATIONAL METHODS

The methods considered to analyze the aerodynamic performance of rotorcraft need to balance solution fidelity with computational cost. Several of these approaches are summarized in Figure 3 as reproduced from Cornelius et al., Ref. [63]. On one end of the spectrum are those methods that model the blades, which have simplifying assumptions enabling fast simulations. Examples of blade-modeled approaches are blade-element momentum theory and actuator-disk methods. These approaches are typically used for a preliminary design; however, if the airfoil characteristics are unknown, or in complex interactions, these modeling methods may not have sufficient fidelity to generate a detailed design. On the other end of the spectrum are blade-resolved approaches, which include blade-resolving CFD methods such as time-accurate Reynolds-averaged Navier-Stokes (RANS), Detached Eddy Simulation (DES), and other hybrid approaches. These approaches are referred to as blade-resolved methods because they solve a form of the Navier-Stokes equations on the true rotor geometry. These high-fidelity analysis methods directly accounting for the blade shape compute the rotor inflow at a much higher computational cost, which in some cases can have a solution time of several weeks. In the middle of the chart, is the Rotorcraft Computational Fluid Dynamics program (RotCFD), Refs. [64-65]. RotCFD is a hybrid approach that combines a blade-modeled description of the rotors with a CFD resolved inflow to achieve accuracy and computational demand suitable for engineering design.

The tool uses a hybrid blade-element momentum theory and unsteady RANS approach. RotCFD captures relevant aspects of the rotor system such as hub and fuselage effects, rotor-rotor interactions, and the full rotor inflow and wake. Key information regarding the tool and prior verification efforts are provided in the reference section, Refs. [64-68].

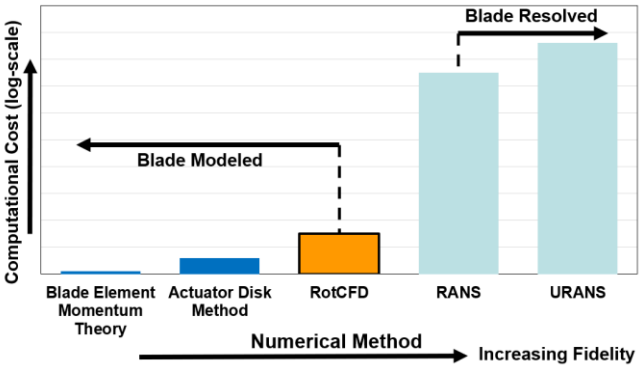

Figure 3. Computational Time vs. Model Fidelity for RotCFD and Other Conventional Approaches, Ref. [63].

GPU Computing with RotCFD

The RotCFD program has the capability to exploit GPU computing. Running the CFD simulations on a GPU accelerated computer can reduce the simulation time from several days or weeks to a few hours. The RotCFD developers have previously documented this capability for a few test cases and available GPUs, Ref. [68]. This study has used two different GPU accelerators: an NVIDIA GTX 1060 (6 GB) and an NVIDIA RTX 3080-Ti. The workstation using the 3080-Ti, which is the fastest commercially available GPU at time of writing, and an AMD Threadripper 3960X 24-core CPU completes these coaxial rotor CFD simulations at 2.5 times the rate of an approximately 1500 processor computing cluster built within the Penn State Department of Aerospace Engineering circa 2016. This highlights the potential performance of a single GPU accelerated workstation. The computing architecture allows for large performance tables to be generated for various activities. One such activity is a look-up table of rotor performance used in flight controllers. RotCFD provides a suitable level of accuracy for the needs of this application while also having a low enough computational cost to complete 800 coaxial CFD simulations in one to two months.

ROTCFD MODEL CREATION

The development of the CFD model has recently been thoroughly documented and is currently under review for publication, Ref. [60]. A short summary of the key developments, however, will be briefly presented here. The first step in creating the CFD model was verification of the provided CAD rotor geometry using a Hexagon RS-6 laser scanner to create a point cloud of the manufactured blade. The point cloud and CAD model were compared using 3D systems Geomagic Control X inspection software. The maximum deviation was 0.9 mm and is depicted in Figure 4.b. Comparisons were also made between the scanned geometry cross-sections and the CAD model cross sections to verify the airfoil shapes along the blade radius. The scanned geometry confirmed the CAD model and the deviations were accepted as negligible.

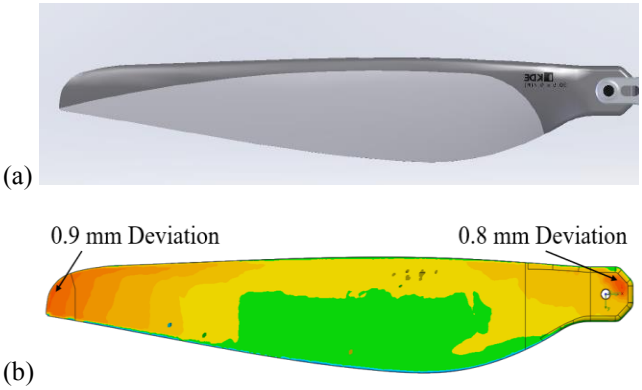

Figure 4. Verification of the KDE 30.5" Rotor Blade Geometry: (a) CAD Model (b) Blade Scan, Ref. [60].

The next step after verifying the CAD model geometry was to discretize the blade into radial stations based on the airfoil distribution and the variation of Reynolds number and Mach number with the radial location, r/R, following the approach by Koning et al., Ref. [69-70]. The airfoil tables are then implemented into the RotCFD program, along with the chord and twist distributions, to model the rotor with the blade element momentum theory (BEMT) method as described previously. Discretizing the rotor blade into stations is essential due to the high variations in the blade performance along the radius of the blade as well as radial changes in airfoil geometry. These variations are dependent on the local airfoil shape, the local Reynolds number, and the local Mach number. For small-scale rotors typical of UAM applications, such as the KDE rotor used in this study, the radial deviation in blade performance characteristics based on these factors can be quite significant. For example, the Reynolds number for this rotor ranges from below one hundred thousand near the root up to nearly five hundred thousand around the 75% span-wise location at the highest throttle setting used. The local Mach number range covers from less than 0.1 up to as high as 0.55. Although the blade tip Mach number can reach as high as 0.55, the inflow and wake velocities in the simulation remain below a Mach number of 0.25. The rotor blade discretization can be seen in Figure 5 and includes a total of ten stations. Five different airfoils were identified along the radius and are referred to as airfoils 1-5 in the figure.

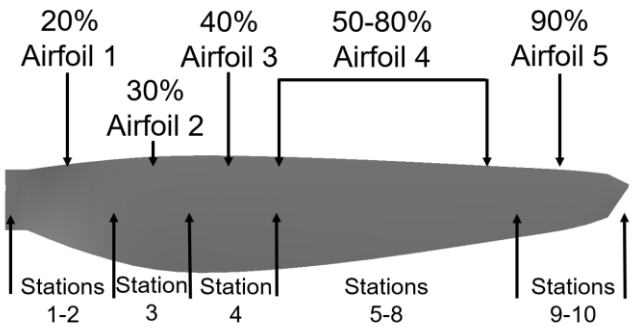

Figure 5. KDE 30.5" Rotor Blade Discretization by Airfoil, Mach, and Reynolds Number, Ref. [60].

A two-dimensional compressible CFD solver, C81 Generator, was used to create the airfoil performance tables for each radial station. The C81 program is a wrapper for the two-dimensional, thin-layer RANS CFD solver, ARC2D, which was originally developed by the U.S. Army's Rotorcraft Group and is currently supported by Sukra Helitek, Inc., Ref [71]. C81 assumes fully-turbulent airfoil performance and an example grid for one airfoil cross section is depicted in Figure 6. For this study, a second set of lower-order free transition airfoil tables was also created with the MIT-XFOIL tool, Ref. [72], to quantify the uncertainty on the rotor performance predictions when using the different sets of airfoil performance tables. This also allows for a check on the C81 fully-turbulent assumption. Although the airfoil drag coefficient increases sharply with fully-turbulent assumed, the input uncertainty in predicted torque is small since the profile power, which is the portion affected by a drag coefficient increase, is roughly one fifth of this rotor's total power. The observed decrease in thrust also reduces the rotor induced power for a given RPM, so the predicted torque is almost unaffected by the fully-turbulent assumption as compared to that of the free-transition. Results comparing the experimental data to simulations using each set of airfoil performance tables will be presented.

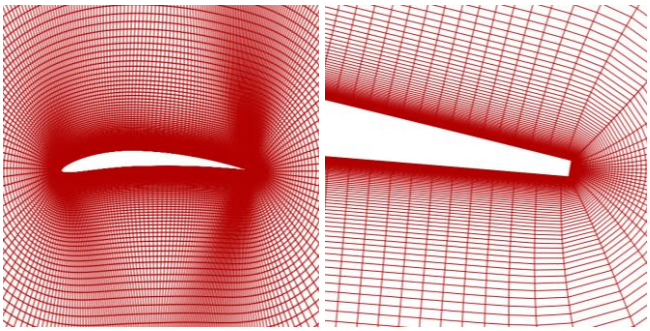

(a) Structured O-grid (b) Blunt Trailing Edge
Figure 6. C81 Grid of a KDE Airfoil Section, Ref. [60].

The C81 Generator simulations were run from an angle-of-attack of -20 through +20 degrees. NACA 0012 experimental data at the appropriate Reynolds number was used to fill in the other angles-of-attack from -180 to +180 deg as an

approximation of airfoil performance beyond stall, where the airfoil performs practically as a flat plate, Ref. [73]. Blending the airfoil performance parameters from the C81 data to the NACA 0012 data was done using the Viterna-Corrigan correction, which is based on an empirical approach for extrapolating post-stall sectional airfoil performance based on flat-plate theory and the rotor dimensions, Refs. [74-75]. The correction was applied immediately after the predicted $C_{l,max}$ value and then blended into the NACA 0012 experimental data. Accurately modeling the airfoil performance at the extreme values of around +/- 180 degrees is important for capturing the proper aerodynamics in the reversed-flow region of the rotor in edge-wise flight. A good airfoil table input deck is also especially important for this work due to the descent conditions explored, such as the vortex ring state (VRS). The lift coefficient versus airfoil angle-of-attack (from -180 to +180 deg) for a sample blade station and rotor speed is depicted in Figure 7. For the free-transition airfoil tables, XFOIL was run from -10 deg through +10 deg angle-of-attack. These values were then overwritten into the existing C81 tables. An example of the resulting free-transition airfoil performance versus the original fully-turbulent C81 data is presented in Figure 8. The free-transition airfoil performance exhibits the expected behavior of a steeper lift-curve slope approaching 2 pi. Comparisons of the drag coefficient vs angle-of-attack are also as expected for most conditions in the normal rotor operating range, which is to say that the free-transition airfoil tables have a lower predicted drag-coefficient. For some of the root sections at low RPM, however, i.e. low Reynolds number, the free-transition simulations predict boundary layer separation at a smaller angle-of-attack. This leads to the predicted free-transition drag coefficient being higher than the fully-turbulent prediction, which has the boundary layer still attached.

Key parameters that were used for the KDE 30.5" rotor were reported in Table 1. The chord and twist distributions that were obtained from the rotor CAD model, as well as the C81 tables that have just been discussed, were added as inputs to finish the rotor description. A front and side view of the RotCFD model are shown in Figure 9.a and 9.b, respectively.

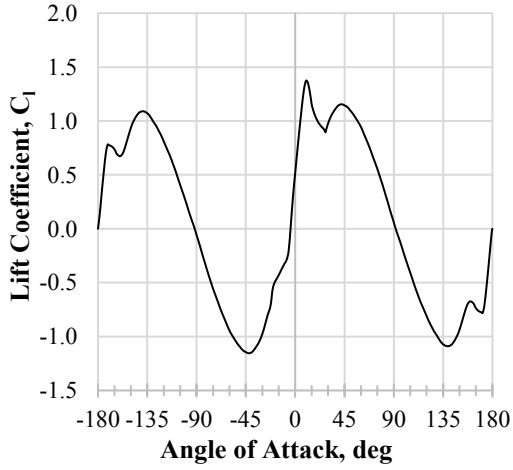

Figure 7. Lift Coefficient vs. Angle-of-Attack for Station 8, Re = 426k, M = 0.43, Ref. [60].

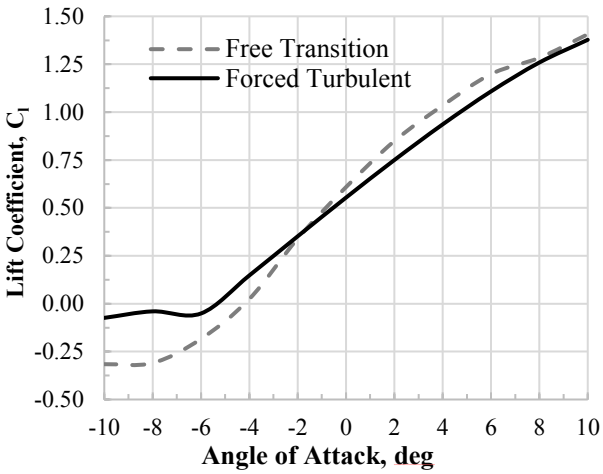

Figure 8. Free vs Forced Transition Airfoil Performance, Station 1, Re = 93k, M = 0.09.

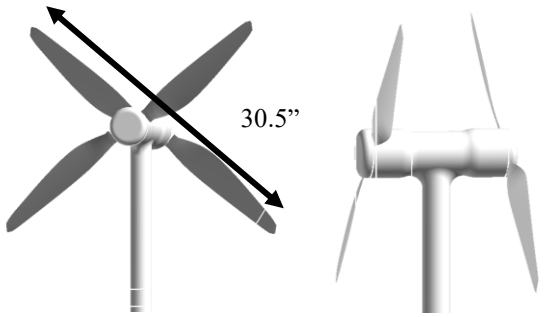

(a) Front View (b) Side View

Figure 9. Views of the RotCFD Model, Ref. [60].

With the rotor description completed, the coaxial rotor model was built. The sting arm and hub regions from Figure 1 are also visible in Figure 8. A rough approximation of this geometry was determined to be helpful in accounting for the interactional aerodynamics present in the wind-tunnel experiment. A grid refinement study was carefully performed that also considered several different approximations of the hub and sting geometry to strike a balance between gridding resolution and computational time per simulation. The final geometry and grid yielded good comparisons with the experimental data while maintaining an acceptable computation time. The grid has approximately 350,000 cells, which is quite small. This is one of the largest advantages of the RotCFD hybrid blade-modeled approach: the flow physics relevant for rotor performance predictions can be accurately modeled without resolving the boundary-layer aerodynamics as is done in conventional blade-resolved CFD.

SINGLE ROTOR RESULTS

The experimental data were measured at 5 kHz. To obtain rotor performance values to compare with the CFD, a moving average approach was used. Post-processing of the data revealed an increasing experimental uncertainty in descent conditions with the maximum in axial-descent. After the rotor thrust and torque were post-processed, they were overlaid with the CFD results as a function of both rotor shaft angle

and throttle setting. Shaft angle, SA, is defined as the angle between the free-stream wind-tunnel velocity and the coaxial rotor system, see Figure 10. A red dot is placed on the upper rotor of the coaxial configuration. For single rotor experimental runs and CFD simulations, the lower rotor was removed.

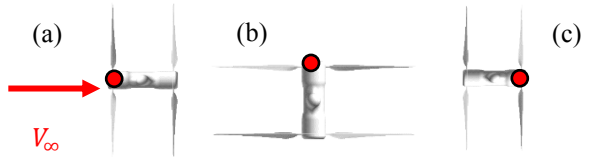

Figure 10. Shaft Angle Definition, Ref. [60].
(a) Axial Climb (SA = -90 deg) (b) Edgewise (SA = 0 deg)
(c) Axial Descent (SA = +90 deg)

Single Rotor: Free- vs Fully-Turbulent Airfoil Tables

Results are presented comparing the single rotor performance of the experimental data with both the free-transition and fully-turbulent airfoil performance tables. Figures 11-12 depict the thrust and torque comparisons, respectively, for a wind-tunnel velocity of 3.81 m/s. Figures 13-14 plot the same information, but for 7.62 m/s. Three throttle conditions are included on each chart, those are the 25, 50, and 75% throttle settings that loosely correspond to about 1600, 2880, and 3900 RPM depending on the shaft angle. The charts represent 36 experimental test conditions and 72 CFD simulations of the single rotor configuration. For most cases, the fully-turbulent airfoil performance tables provide better correlation with the experimental thrust data. Results for the torque comparisons are less consistent in trend, which indicates that the impact on torque of the decreased drag coefficient for the free-transition airfoil tables is negated by the increase in rotor thrust associated with the steeper lift-curve slope seen in Figure 8. Since thrust is thus the more sensitive parameter, the fully-turbulent C81 airfoil performance tables are deemed the better fit to the experimental data and the better representation of the flow physics.

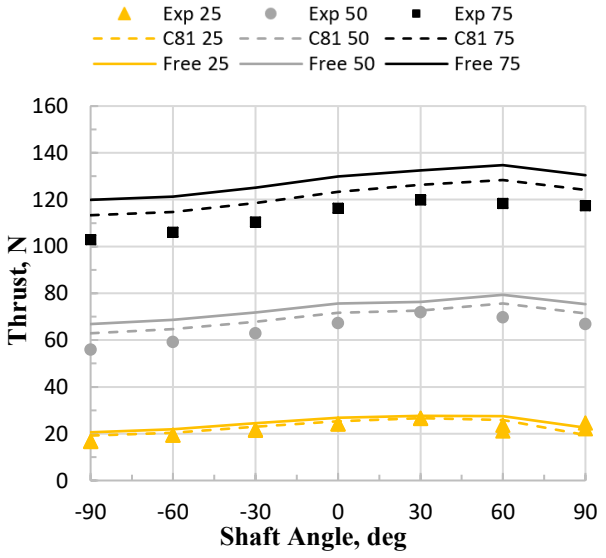

Figure 11. Single Rotor Thrust, Free- vs Fully-Turbulent Airfoil Tables, V = 3.81 m/s

This result could be counter-intuitive since the low Reynolds numbers would suggest some portion of the airfoil chord to be experiencing laminar flow. The complex flow conditions, however, of this small-scale, high tip-speed rotor system could be responsible for early transition and one explanation as to why the fully-turbulent airfoil performance tables correlate better with the experimental data than the free-transition tables.

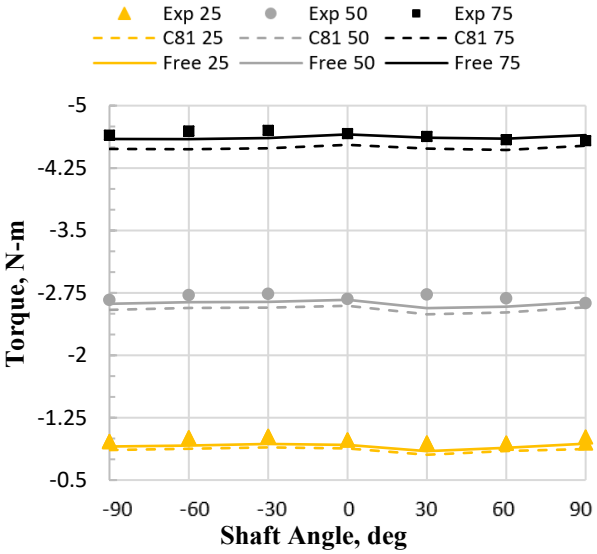

Figure 12. Single Rotor Torque, Free- vs Fully-Turbulent Airfoil Tables, V = 3.81 m/s.

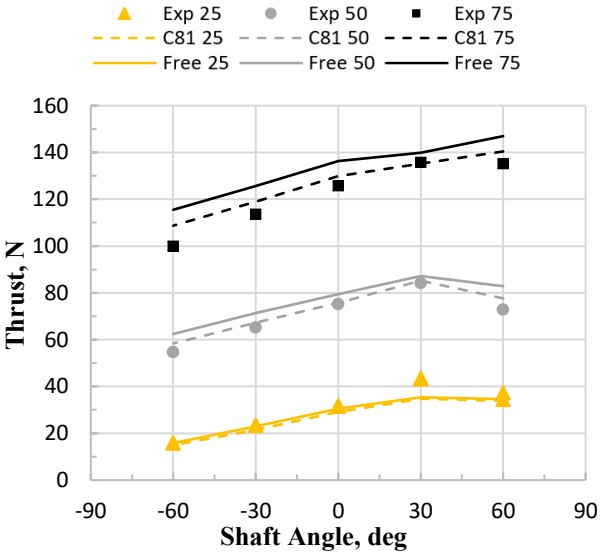

Figure 13. Single Rotor Thrust, Free- vs Fully-Turbulent Airfoil Tables, V = 7.62 m/s.

Of special note when viewing these charts is that the experimental uncertainty values increase when moving to the higher shaft angles, which are representative of descent conditions. The uncertainty values are very well documented in Ref. [60], but the primary conclusion is that the complex flowfields of vortex ring state (VRS), turbulent wake state (TWS), and the windmill brake state (WBS) create challenging test conditions in the wind tunnel. Still, the

average deltas ($(CFD - EXP)/EXP$) are within 4% for both thrust and torque. Table 2 further summarizes the deltas of the simulations to the experimental data by flight condition. For the C81 airfoil tables, climb conditions have the largest thrust discrepancy at 6% (over-predicted) and the descent conditions have the largest torque discrepancies at -5.5% (under-predicted). The average torque delta of the free-transition model is lower, but the corresponding average thrust delta is much higher at 9.5%. In this work, thrust is typically deemed the more important parameter for which to reduce prediction uncertainty.

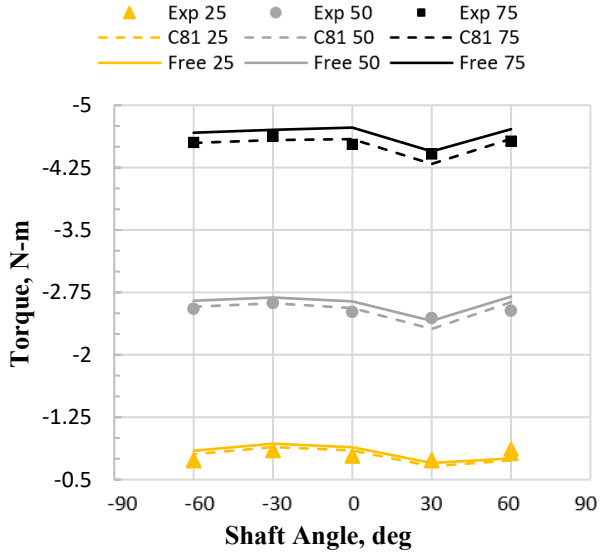

Figure 14. Single Rotor Torque, Free- vs Fully-Turbulent Airfoil Tables, V = 7.62 m/s.

Table 2. Single Rotor Comparisons to Experimental Data for C81 (Fully-Turbulent) and Free (Free-Transition) Airfoil Performance Tables.

Flight Condition	C81 Thrust	C81 Torque	Free Thrust	Free Torque
Total	3.6%	-3.9%	9.5%	-0.5%
Climb	6%	-3.5%	12.6%	-0.2%
Edgewise	2.2%	-0.8%	7.6%	2.7%
Descent	1.8%	-5.5%	7.1%	-1.9%

COAXIAL ROTOR RESULTS

This section begins with a similar analysis comparing rotor performance predictions of the coaxial rotor system to experimental data when using free-transition versus fully-turbulent airfoil tables. Simulation results are then presented that compare the rotor performance predictions of the single rotor model to both the upper and lower rotors of the coaxial model versus shaft angle.

Coaxial Rotor: Free- vs Fully-Turbulent Airfoil Tables

A similar analysis comparing the CFD rotor performance predictions, using both free-transition and fully-turbulent airfoil tables, to the experimental data was conducted. The results are reported in Figures 15-16 for the upper and lower rotor thrust, respectively, and Figures 17-18 for the upper and lower rotor torque, respectively. These data for the coaxial rotor system are at a wind-tunnel velocity of 6.1 m/s, compared to the single rotor cases at 3.81 and 7.62 m/s. Only simulations of the 25% and 75% throttle conditions were completed, and are depicted in the figures along with the corresponding experimental data.

For the coaxial rotor thrust in Figures 15-16, the trends of free-transition versus fully-turbulent simulations are the same as for the single rotor cases. The free-transition airfoil performance tables still have the same higher lift-curve slopes, which results in a higher thrust coefficient and thrust value for all other settings held constant. This is explained by the relationship between thrust coefficient and average rotor lift coefficient. Of special interest in Figure 16 is the reversal of the trends for C81 25 versus Free 25 in a high rate of descent, i.e. SA = +45 to +90. At the low Reynolds numbers associated with this rotor, a fully-turbulent assumption keeps the boundary layer attached to the airfoil until higher angles-of-attack as compared to the free-transition performance. This combination of low rotor speed and high rate of descent, along with the observed reversal in the trend of predicted thrust, indicates the lower rotor is approaching stall in this region, and thus the free-transition airfoil tables would have a lower airfoil lift coefficient. Comparing this to the upper rotor in Figure 15 at the same conditions, the same phenomenon does not appear to be present. This highlights the vortex ring state (VRS) shielding phenomenon of the upper rotor by the lower rotor, which has been observed in past studies of similar coaxial rotor systems, Refs. [34, 36, 60]. One of those past works observed similar features in higher-fidelity blade-resolved CFD of a coaxial rotor system. Basically, the lower rotor of a coaxial rotor system delays the onset of VRS conditions for the upper rotor to higher rates of descent. This will be discussed again later.

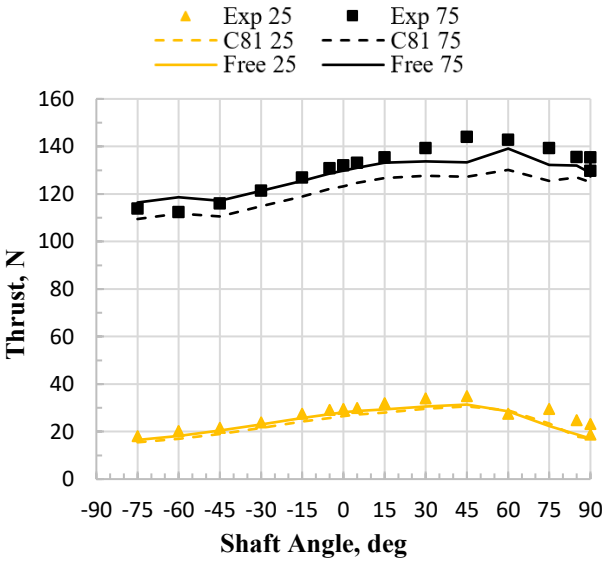

Figure 15. Coaxial Rotor Thrust (Upper), Free- vs Fully-Turbulent Airfoil Tables, V = 6.1 m/s.

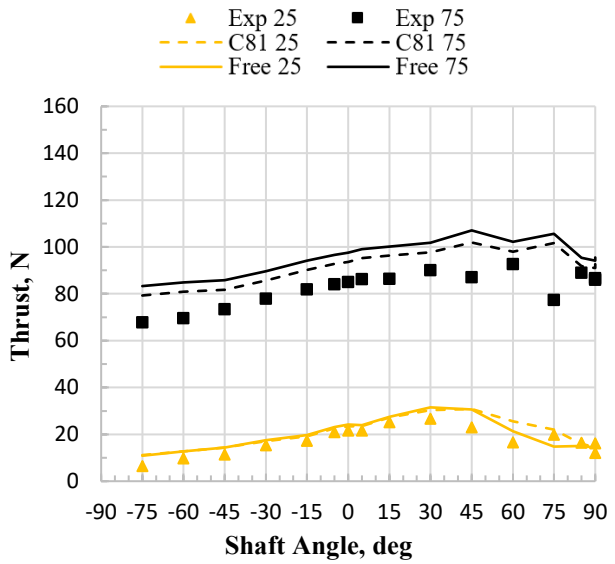

Figure 16. Coaxial Rotor Thrust (Lower), Free- vs Fully-Turbulent Airfoil Tables, V = 6.1 m/s.

The comparisons of predicted torque to the experimental data are in Figures 17 and 18. The trends are again consistent with the single rotor analyses in that the free-transition simulations predict an overall higher magnitude of rotor torque. Again, this is due to the fact that the free-transition simulations are producing more thrust (prior to stall in high shaft angle descent conditions), which results in higher induced power (hence torque) and drives the result. The relative deltas $((CFD - EXP)/EXP)$ between simulation and experimental results for the upper and lower rotors are reported in Tables 3 and 4, respectively. In general, the upper rotor thrust is under-predicted by the fully-turbulent airfoil tables, and the lower rotor thrust is over-predicted. The free-transition values have similar trends, but the under-prediction of the upper rotor thrust is slightly decreased and the over-prediction of the lower rotor thrust is increased. The torque predictions for all simulations are over-predicted, with the fully-turbulent predictions consistently providing a better correlation to the experimental data.

Table 3. Coaxial Rotor Comparisons (Upper) to Experimental Data for C81 (Fully-Turbulent) and Free (Free-Transition) Airfoil Performance Tables.

Flight Condition	C81 Thrust	C81 Torque	Free Thrust	Free Torque
Total	-6.5%	2.6%	-4.5%	6.5%
Climb	-5.4%	0.5%	-2.3%	3.8%
Edgewise	-6.9 %	2.6%	-3.3%	9.6%
Descent	-6.4%	3.6%	-7.2%	7.8%

Given the strong correlation of the single rotor experimental data with the fully-turbulent simulations, it is interesting, though not completely unexpected, to observe larger deltas in the coaxial comparisons. The rotor flow state is much more complex, and likely leads to the additional discrepancies. It appears the lower rotor may be inducing a stronger than realistic inflow at the upper rotor that acts to reduce the upper rotor predicted thrust in Figure 15. Also, the upper rotor wake that convects into the lower rotor appears to be too weak, which makes sense since the upper rotor thrust is under-predicted. Hence the lower rotor thrust is over-predicted (see Figure 16).

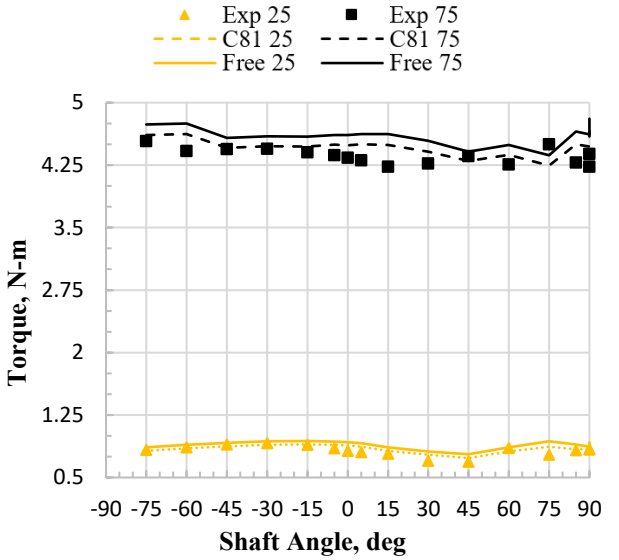

Figure 17. Coaxial Rotor Torque (Upper), Free- vs Fully-Turbulent Airfoil Tables, V = 6.1 m/s.

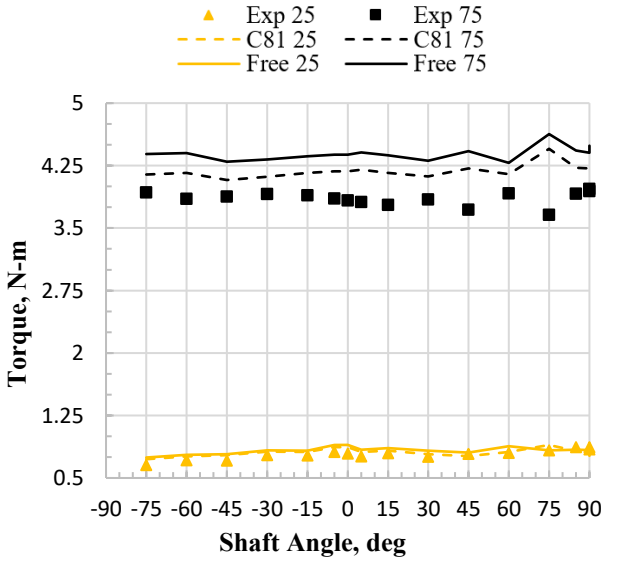

Figure 18. Coaxial Rotor Torque (Lower), Free- vs Fully Turbulent Airfoil Tables, V = 6.1 m/s.

Table 4. Coaxial Rotor Comparisons (Lower) to Experimental Data for C81 (Fully-Turbulent) and Free (Free-Transition) Airfoil Performance Tables.

Flight Condition	C81 Thrust	C81 Torque	Free Thrust	Free Torque
Total	14.8%	6.7%	15.5%	9.7%
Climb	16.1%	5.5%	21.2%	11.1%
Edgewise	11.0%	7.6%	13.5%	13.7%
Descent	16.9%	6.9%	12.2%	8.5%

Comparisons of the total coaxial rotor thrust were also made and are reported in Figure 19, with the deltas summarized in Table 5. The average coaxial rotor thrust delta is 1.4% across all conditions for the fully-turbulent simulations, which is more in line with the single rotor results. This is an outcome of the discrepancies for both the upper and lower rotor thrust predictions cancelling out in a fortuitous way. The coaxial rotor power is also in better agreement for the fully-turbulent simulations, which solidifies the C81 model as the better fit.

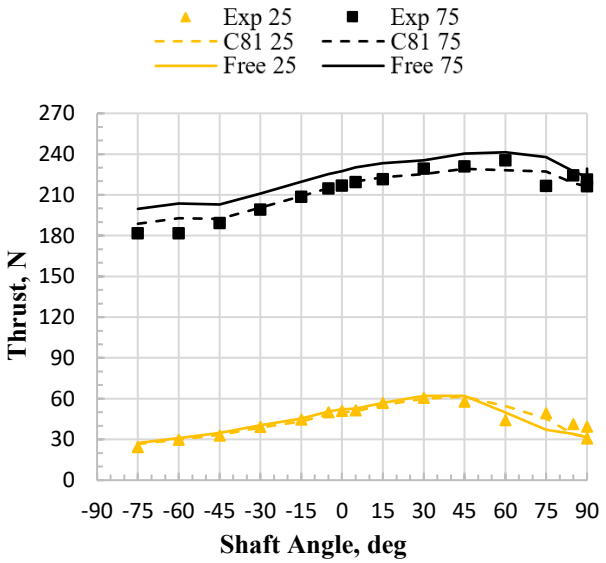

Figure 19. Combined Coaxial Rotor Thrust, Free- vs Fully-Turbulent Airfoil Tables, V = 6.1 m/s.

Table 5. Combined Coaxial Rotor Thrust Comparisons to Experimental Data for C81 (Fully-Turbulent) and Free (Free-Transition) Airfoil Performance Tables.

Flight Condition	C81 Thrust	Free Thrust
Total	1.4%	3.0%
Climb	2.3%	7.4%
Edgewise	0.0%	3.5%
Descent	2.0%	0.4%

Single vs Coaxial Rotor: Fully-Turbulent Airfoil Tables

Since the previously reported single rotor and coaxial rotor test conditions were unfortunately not acquired at the same wind-tunnel speeds, the results are best non-dimensionalized in order to compare between the two configurations. The single rotor test conditions were conducted as a subset of the test matrix after the full coaxial rotor test matrix was completed. Additionally, the throttle settings each had different results due to the changing proportion of rotor thrust as compared to the energy in the oncoming flow. Within each throttle grouping, the method of controlling rotor speed with throttle also leads to some deviation in the rotor RPM as a function of the wind-tunnel test condition. Non-dimensionalizing the thrust coefficients further helps to remove these discrepancies. Here the comparisons are shown as a function of shaft angle to highlight the differences based on flight condition, i.e. climb, edgewise flight, and descent.

Figure 20 depicts the predicted single and coaxial rotor thrust coefficients at the 75% throttle setting, plotted against shaft angle. The predictions are from the RotCFD models with the fully-turbulent airfoil performance tables, which are used for the remainder of this discussion. Of special interest is that the single rotor data closely approximates the upper rotor performance of the coaxial rotor system. In forward flight conditions (SA = -30 to 0 deg), this could be expected with some small discrepancy due to the presence of the lower rotor beneath the upper rotor, but in these conditions the rotor-rotor interaction is small and the upper rotor in the coaxial configuration mostly encounters undisturbed inflow. For steep climb conditions (SA = -90 to -45 deg), the single rotor predicted thrust coefficient is a bit higher than the coaxial upper rotor. This is likely due to the fact that in a climb condition, the wake skew angle is small and the rotor-rotor interaction is high. Thus, the upper rotor in these conditions is affected by the presence of the lower rotor.

What is more interesting, however, is this comparison for other flight conditions such as descent, which corresponds to shaft angles of +5 deg and greater, with axial descent at +90 deg. Beyond +30 deg, which is the start of the 'high rate of descent' region, the upper rotor is influenced much more by the presence of the lower rotor. Depending on the particular throttle setting and flight speed, the lower rotor can exhibit blockage effects on the upper rotor and lead to large rotor-rotor interactions that affect each rotor's performance. For the 75% throttle condition of Figure 20, however, the ratio of induced velocity to flight speed is large enough that even the descent conditions do not cause abrupt shifts in the thrust coefficient. For this particular case, the single rotor performance is still a good predictor of the coaxial rotor's upper rotor performance even in descent conditions.

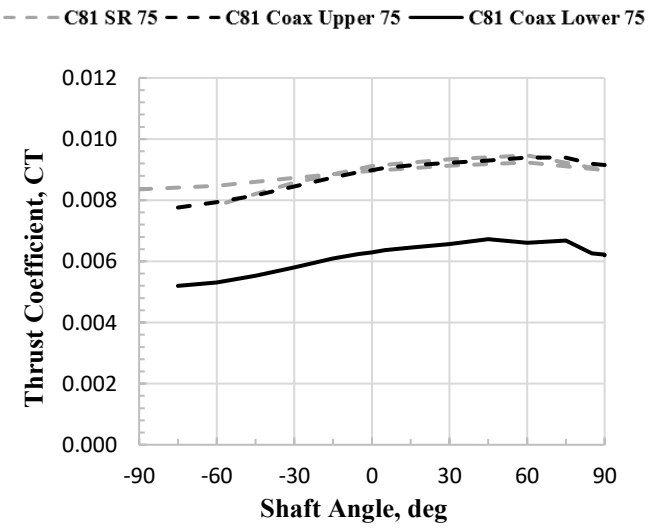

Figure 20. Single and Coaxial Rotor Thrust Coefficient vs Shaft Angle, 75% Throttle.

The same information for the 25% throttle setting is presented in Figure 21. The lower induced velocity at the same wind-tunnel speeds result in the rotor performance being affected much more by the oncoming wind-tunnel flow. The degree to

which the flow affects the rotor performance is a function of the rotor shaft angle, which determines the individual rotor wake skew angle and the magnitude of the wind-tunnel flow velocity normal to the rotor disk. In climb conditions (SA = -90 to -30 deg), the flow normal to the rotor disk acts to reduce the thrust coefficient for all cases. For forward flight and edgewise cases (SA = -15 to 0 deg), the oncoming wind-tunnel velocity is clearing the upper rotor wake from the lower rotor, i.e. a large wake-skew angle. As descent conditions are approached (SA = +15 to +45 deg), the rotors begin to be affected by VRS conditions. Of special note is that the lower rotor in Figure 21 is highly affected by VRS conditions in this region, while the upper rotor VRS effects are delayed to a higher shaft angle, which can be thought of as a higher rate of descent if considering flow normal to the rotor disk. At still higher shaft angles approaching axial descent (SA = 60 to 90 deg), the lower rotor thrust coefficient begins again trending upward, signifying a crossover to the turbulent wake state or windmill brake state conditions and stalled rotor performance.

The single rotor performance initially tracks closely with the upper rotor of the coaxial configuration. At higher shaft angles, however, the two start to differ. For this particular combination of wind-tunnel velocity and throttle setting, the single rotor achieves a higher thrust coefficient in the early stages of descent (SA = 0 to +30 deg), which can be attributed to the fact that there is no lower rotor shielding it from the oncoming flow. As the shaft angle increases, which again can be thought of as higher rates of descent for a fixed speed, the thrust coefficient changes trend at +30 deg. This indicates the onset of the VRS effects at a lower shaft angle, or lower rate of descent, as compared to the upper rotor of the coaxial configuration with a notable change in trend at +60 deg.

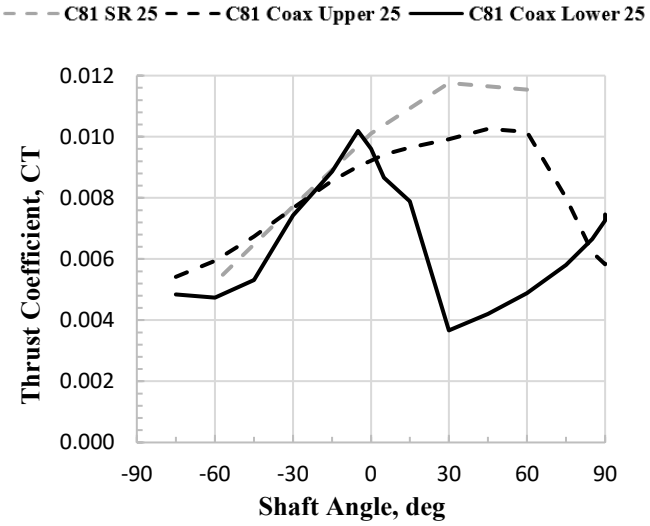

Figure 21. Single and Coaxial Rotor Thrust Coefficient vs Shaft Angle, 25% Throttle.

CONCLUSIONS

This paper presented an introductory analysis of single versus coaxial rotor performance predictions and performance based on RotCFD computations and available data.

The objectives of this work were to:

1. Summarize major developments in an efficient CFD model for multi-rotor performance prediction.
2. Document the effects of using fully-turbulent (forced transition) versus free-transition airfoil tables on CFD rotor performance predictions.
3. Compare single versus coaxial rotor thrust across a wide range of flight conditions.

Discussion on the first objective presented the RotCFD model development and best practices used for predicting both single and coaxial rotor performance. A brief background of the CFD tool was also provided to place it in context with other common rotor performance prediction approaches. A brief description of the tool's advantages with respect to GPU accelerated computing was also provided.

To meet the second objective, RotCFD simulations for both the single and coaxial rotor models were carefully conducted using two different sets of airfoil performance tables. The first set of tables was generated with the C81 Generator tool, which is a two-dimensional thin-layer RANS flow solver used to generate fully-turbulent airfoil performance. The process of building complete airfoil performance tables that range from -180 deg to +180 deg angle-of-attack was also discussed. These tables use NACA 0012 experimental data beyond stall, where the airfoil performance approximates that of a flat plate. The C81 data was blended into the NACA 0012 data using the Viterna-Corrigan correction, which is an approximation based on the rotor geometry. The second set of airfoil performance tables used a free-transition assumption from -10 deg to +10 deg angle-of-attack, and were generated using MIT-XFOIL. The CFD data were then compared to experimentally obtained wind tunnel data from the NASA Langley 14- by 22- ft. Subsonic Tunnel Facility. For the single rotor cases, the average total thrust and torque discrepancies between the experimental data and the CFD simulations using the fully-turbulent airfoil performance tables was less than 4%. It was found that the impact on torque of the decreased drag coefficient for the free-transition airfoil tables is negated by the increase in rotor thrust from the steeper lift-curve slope at these operating Reynolds numbers.

For the coaxial rotor simulations, the torque was found to be over-predicted for all simulations, and the fully-turbulent airfoil tables gave a better correlation to the experimental data. The thrust comparisons were a bit more complex. For the fully-turbulent airfoil table simulations, the upper rotor thrust was under-predicted and the lower rotor thrust was over-predicted. The combined coaxial rotor thrust, however, was very well predicted. The free-transition airfoil table simulations led to higher values of thrust, in general, and thus slightly improved the upper rotor correlation but worsened the lower rotor results. The average coaxial rotor thrust and torque comparisons using the fully-turbulent airfoil tables were within 1.4% and 3% of the experimental values, respectively.

The last objective of this work was to compare single versus coaxial rotor performance across a wide range of flight

conditions. In this work, that is interpreted as axial-climb (SA = -90 deg), through edgewise flight (SA = 0 deg), to axial-descent (SA = +90 deg). Comparisons were made between the single and coaxial rotor models using the fully-turbulent airfoil performance tables. From results on the individual rotor thrust coefficient, it was observed that the single rotor can be a good approximation of the upper rotor performance in a coaxial rotor configuration with notable rotor spacing as presented in this work and considered for some UAM applications. This can be true across most flight conditions if the rotor induced velocity is large compared to the flight speed. For larger flight speeds, on the other hand, there are regions where the behavior changes. Results at the 25% throttle setting showed that all rotors behave similarly in forward flight where the rotor-rotor interaction is small due to the large rotor spacing and large wake skew angle. For descent conditions (SA = 0 deg and higher), however, the individual rotor performance can greatly differ. The onset of VRS conditions, for example, was delayed to a higher shaft angle for the upper rotor. A higher shaft angle can also be thought of as a higher rate of descent, or velocity normal to the rotor disk, for a shaft angle sweep at constant wind-tunnel speed. These observations agree with past studies that observed similar features.

This work provided further verification for the single and coaxial rotor RotCFD models developed. The correlations with experimental data appear to be better when using the fully-turbulent airfoil performance tables for this particular rotor and operating conditions. Further investigation is required to resolve the slightly larger discrepancies in the individual upper and lower rotor thrust values as compared to the experimental data. Still, the coaxial rotor thrust and torque values showed an average agreement within 1.4% and 3% respectively.

Author contact: Jason K. Cornelius joc5693@psu.edu

ACKNOWLEDGMENTS

This research effort is funded through the NASA New Frontiers Program. The authors would like to extend their gratitude to William Polzin and Rs Nappinnai of Sukra Helitek Incorporated for their continued support as well as the late Dr. Ganesh Rajagopalan for his contributions enabling increased access to the CFD analysis tool used in this work. Additionally, the authors would like to thank Witold Koning, Larry Young, Ethan Romander, and Dr. William Warmbrodt of the NASA Ames Research Center for their guidance. Lastly, a big thank you to Kirk Heller and Ben Enders at Penn State University for their assistance in developing high performance GPU computing capabilities used in this work.

REFERENCES

1. Cheney, M. C., "The ABC Helicopter," AIAA Paper No. 69-217, AIAA/AHS VTOL Research, Design, and Operations Meeting, Feb. 17-19, 1969. https://doi.org/10.2514/6.1969-217
2. Ruddell, A. J., "Advancing Blade Concept (ABC) Development," AHS Journal, Vol. 22, No. 1, Jan. 1977, pp. 13-23. https://doi.org/10.4050/JAHS.22.1.13
3. Fegely, C., Juhasz, O., Xin, H., Tischler, M., "Flight Dynamics and Control Modeling with System Identification Validation of the Sikorsky X2 Technology Demonstrator," AHS 72nd Annual Forum, May 17-19, 2016. https://nams.usra.edu/sites/nams/assets/AFDD/AHS_2016_Fegely.pdf
4. Feil, R., Eble, D., Hajek, M., "Comprehensive Analysis of a Coaxial Ultralight Rotorcraft and Validation with Full-Scale Fligth Test Data," AHS Journal, Vol. 63, No. 4, pp. 1-12, Oct. 2018. https://doi.org/10.4050/JAHS.63.042004
5. Feil, R., Hajek, M., "Aeromechanics of a Coaxial Ultralight Rotorcraft During Turn, Climb, and Descent Flight," AIAA Journal of Aircraft, Published Online July 2020. https://doi.org/10.2514/1.C035684
6. Diaz, P. V., Rubio, R. C., Yoon, S., "Simulations of Ducted and Coaxial Rotors for Air Taxi Operations," AIAA Aviation Forum, June 17-21, 2019. https://doi.org/10.2514/6.2019-2825
7. Brown, A., Harris, W., "Vehicle Design and Optimization Model for Urban Air Mobility," AIAA Journal of Aircraft, Vol. 57, No. 6, Nov.-Dec. 2020. https://doi.org/10.2514/1.C035756
8. Shrestha, R., Benedict, M., Hrishikeshavan, V., Chopra, I., "Hover Performance of a Small-Scale Helicopter Rotor for Flying on Mars," AIAA Journal of Aircraft, Vol. 53, No. 4, July-Aug. 2016. https://doi.org/10.2514/1.C033621
9. Grip, H., Johnson, W., Malpica, C., Scharf, D., Mandic, M., Young, L., Allan, B., Mettler, B., Martin, M., Lam, J., "Modeling and Identification of Hover Flight Dynamics for NASA's Mars Helicopter," AIAA Journal of Guidance, Control, and Dynamics, Vol. 43, No.2, Feb. 2020. https://doi.org/10.2514/1.G004228
10. Gessow, A., "Effect of Rotor-Blade Twist and Plan-Form Taper on Helicopter Hovering Performance," NACA TN-1542, Feb. 1948. https://ntrs.nasa.gov/citations/19930082219
11. Harrington, R., "Full-Scale Investigation of the Static-Thrust Performance of a Coaxial Helicopter Rotor," NACA TN-2318, March 1951. https://ntrs.nasa.gov/citations/19930083001
12. Dingeldein, R., "Wind-Tunnel Studies of the Performance of Multirotor Configurations," NACA TN-3236, Aug. 1954. https://ntrs.nasa.gov/citations/19930083899
13. Coleman, C., "A Survey of Theoretical and Experimental Coaxial Rotor Aerodynamic Research," NASA TP-3675, March 1997. https://ntrs.nasa.gov/citations/19970015550
14. Ramasamy, M., "Hover Performance Measurements Toward Understanding Aerodynamic Interference in Coaxial, Tandem, and Tilt Rotors," Journal of the American Helicopter Society, Vol. 60, No. 3, pp. 1-17. https://doi.org/10.4050/JAHS.60.032005

15. Yeo, H., "Design and Aeromechanics Investigation of Compound Helicopters," Aerospace Science and Technology, Vol. 88, 2019, pp. 158-173. https://doi.org/10.1016/j.ast.2019.03.010
16. Silva, C., Johnson, W., Solis, E., "Concept Vehicles for VTOL Air Taxi Operations," AHS Technical Meeting on Aeromechanics Design for Vertical Lift, Holiday Inn at Fisherman's Wharf, San Francisco, CA, Jan. 16-18, 2018. https://rotorcraft.arc.nasa.gov/Publications/files/Johnson_2018_TechMx.pdf
17. Silva, C., Johnson, W., Antcliff, K.R., and Patterson, M.D., "VTOL Urban Air Mobility Concept Vehicles for Technology Development," 2018 Aviation Technology, Integration, and Operations Conference, AIAA Aviation Forum, AIAA 2018-3847, Dallas, TX, June 2018. https://doi.org/10.2514/6.2018-3847
18. Antcliff, K., Whiteside, S., Kohlman, L., and Silva, C., "Baseline Assumptions and Future Research Areas for Urban Air Mobility Vehicles," AIAA SciTech, AIAA-2019-0528, May 28, 2019. https://doi.org/10.2514/6.2019-0528
19. Silva, C., Johnson, W., "Practical Conceptual Design of Quieter Urban VTOL Aircraft," Presented at the Vertical Flight Society's 77th Annual Forum & Technology Display, Virtual, May 10–14, 2021. https://rotorcraft.arc.nasa.gov/Publications/files/77-2021-0202_Silva.pdf
20. Johnson W. and Silva C., "NASA concept vehicles and the engineering of advanced air mobility aircraft," The Aeronautical Journal, 2021, pp. 1-33. https://doi.org/10.1017/aer.2021.92
21. Russell, C., Willink, G., Theodore, C., Jung, J., and Glasner, B., "Wind Tunnel and Hover Performance Test Results for Multicopter UAS Vehicles," NASA/TM02018-219758, Feb. 2018. https://rotorcraft.arc.nasa.gov/Publications/files/Russell_1180_Final_TM_022218.pdf
22. Gregory, D., Cornelius, J.,Waltermire, S., Loob, C., and Schatzman, N., "Acoustic Testing of Five Multicopter UAS in the U.S. Army 7- by 10-Foot Wind Tunnel," NASA/TM-2018-219894, May 2018, https://rotorcraft.arc.nasa.gov/Publications/files/Schatzman_TM_2018_219894_Final.pdf
23. Yoon, S., Diaz, P., Boyd, D., Chan, W., and Theodore, C., "Computational Aerodynamic Modeling of Small Quadcopter Vehicles," AHS 73rd Annual Forum, May 2017. https://rotorcraft.arc.nasa.gov/Publications/files/73_2017_0015.pdf
24. Wright, S. J., "Fundamental Aeroelastic Analysis of an Urban Air Mobility Rotor," Presented at the Vertical Flight Society's 9th Biennial Autonomous VTOL Technical Meeting, Virtual, January 26-28, 2021. https://rotorcraft.arc.nasa.gov/Publications/files/WRIGHT_EVTOL_2021_FINAL_REVISED2.pdf
25. Conley, S., Shirazi, D., "Comparing Simulation Results from CHARM and RotCFD to the Multirotor Test Bed Experimental Data," Presented 2021 AIAA Aviation Forum Virtual Event August 2-6, 2021. https://rotorcraft.arc.nasa.gov/Publications/files/CHARM_RotCFD_Test_Bed_Data_AIAA_Conley_Shirazi.pdf
26. Withrow–Maser, S., Malpica, C., Nagami, K., "Impact of Handling Qualities on Motor Sizing for Multirotor Aircraft with Urban Air Mobility Missions," Presented at the Vertical Flight Society's 77th Annual Forum & Technology Display, Virtual, May 10-14, 2021. https://rotorcraft.arc.nasa.gov/Publications/files/Impact_of_Handling_Qualities_on_Motor_Sizing_for_Multirotor_Aircraft_with_Urban_Air_Mobility_Missions_final.pdf
27. Beiderman, P.R., Darmstadt, C.D., Silva C., "Hazard Analysis Failure Modes, Effects, and Criticality Analysis for NASA Revolutionary Vertical Lift Technology Concept Vehicles," Presented at the Vertical Flight Society's 77th Annual Forum And Technology Display, Virtual, May 10–14, 2021. https://rotorcraft.arc.nasa.gov/Publications/files/77-2021-0287_Beiderman.pdf
28. Cummings, H., Willink, G., Silva C., "Mechanical Design of the Urban Air Mobility Side-by-Side Test Stand," Presented at the Vertical Flight Society's 9th Biennial Autonomous VTOL Technical Meeting, Virtual, January 26-28, 2021. https://rotorcraft.arc.nasa.gov/Publications/files/MechanicalDesignoftheUAMSBSTestStand_Cummings_AutonomousVTOLMeeting_.pdf
29. Orazio, P., Oberai, A., Healy, R., Niemiec, R., Gandhi, F., "Multi-Fidelity Surrogate Model for Interactional Aerodynamics of a Multicopter," Vertical Flight Society Annual Forum 77, 2021.
30. Walter, A., Niemiec, R., Gandhi, F., "Effects of Disk Loading on Handling Qualities of Large-Scale, Variable-RPM Quadcopters," Vertical Flight Society Annual Forum 77, 2021.
31. Healy, R., Gandhi, F., Mistry, M., "Computational Investigation of Multirotor Interactional Aerodynamics with Hub Lateral and Longitudinal Canting," *AIAA Journal,* published online Sept. 28, 2021. https://doi.org/10.2514/1.J060530
32. Healy, R., Misiorowski, M., Gandhi, F., "A CFD-Based Examination of Rotor-Rotor Separation Effects on Interactional Aerodynamics for eVTOL Aircraft," *Journal of the American Helicopter Society,* Vol. 67, 2022. https://doi.org/10.4050/JAHS.67.012006
33. Bahr, M., McKay, M., Niemiec, R., and Gandhi, F., "Handling qualities of fixed-pitch, variable-speed multicopters for urban air mobility," *The Aeronautical Journal*, 2021. https://doi.org/10.1017/aer.2021.114
34. Cornelius, J., Opazo, T., Schmitz, S., Langelaan, J., Villac, B., Adams, D., Rodovskiy, L., Young, L., "Dragonfly – Aerodynamics during Transition to Powered Flight," VFS 77th Annual Forum, May, 2021. https://rotorcraft.arc.nasa.gov/Publications/files/77-2021-0264_Cornelius.pdf

35. Opazo, T., and Langelaan, J., "Longitudinal control of transition to powered flight for a parachute dropped multi-copter," AIAA SciTech Forum, AIAA 2020-2072. https://doi.org/10.2514/6.2020-2072
36. Kinzel, M. P., Cornelius, J. K., Schmitz, S., Palacios, J. L., Langelaan, J. W., Adams, D. S., Lorenz, R. D., "An Investigation of the Behavior of a Coaxial Rotor in Descent and Ground Effect," AIAA SciTech Forum, Jan. 2019. https://arc.aiaa.org/doi/pdf/10.2514/6.2019-1098
37. Deluane, J., Izraelevitz, J., Sklyanskiy, E., Schutte, A., Fraeman, A., Scott, V., Leake, C., Ballesterost, E., Aaron, K., Young, L., Johnson, W., Withrow-Maser, S., Cummings, H., Bhagwat, R., Veismann, M., Wei, S., Lee. R., Pabon Madrid, L., Morteza, G., Burdick, J., Rapin, W., "Motivations and Preliminary Design for Mid-Air Deployment of a Science Rotorcraft on Mars " Presented at the AIAA Ascend Conference, Virtual, November 16–18, 2020. https://rotorcraft.arc.nasa.gov/Publications/files/Mid_Air_Deployment_Delaune.pdf
38. Veismann, M., Wei, S., G., Conley, S., Young, L., Delaune, J., Burdick, J., Gharib, M., Izraelevitz, J., "Axial Descent of Variable-Pitch Multirotor Configurations: An Experimental and Computational Study for Mars Deployment Applications," Presented at the Vertical Flight Society's 77th Annual Forum & Technology Display, Virtual, May 10–14, 2021. https://rotorcraft.arc.nasa.gov/Publications/files/77-2021-0193_Veismann.pdf
39. Niemiec, R., Gandhi, F., Kopyt, N., "Relative rotor phasing for multicopter vibratory load minimisation," *The Aeronautical Journal,* 2021. https://doi.org/10.1017/aer.2021.94
40. Cornelius, J., Zhang, J., Schmitz, S., Smith, E., "Comprehensive Analysis of Coaxial Rotor Dynamics on a Support Arm," AIAA Science and Technology Forum, San Diego, Jan. 2022. AIAA 2022-0930. https://doi.org/10.2514/6.2022-0930
41. Grip, H., Johnson, W., Malpica, C., Scharf, D., Mandic, M., Young, L., Allan, B., Mettler, B., Martin, M., Lam, J., "Modeling and Identification of Hover Flight Dynamics for NASA's Mars Helicopter," AIAA Journal of Guidance, Control, and Dynamics, Vol. 43, No.2, Feb. 2020. https://doi.org/10.2514/1.G004228
42. Balaram, J., Canham, T., Duncan, C., Golombek, M., Grip, H., Johnson, W., Maki, J., Quon, A., Stern, R., Zhu, D., "Mars Helicopter Technology Demonstrator," AIAA SciTech Forum, Kissimmee, Florida, 2018. https://doi.org/10.2514/6.2018-0023
43. Koning, W., Johnson, W., and Grip, H., "Improved Mars Helicopter Aerodynamic Rotor Model for Comprehensive Analyses," AIAA Journal, Vol. 57, No. 9, Sept. 2019. https://doi.org/10.2514/1.J058045
44. Koning, W., "Generation of Performance Model for the Aeolian Wind Tunnel (AWT) Rotor at Reduced Pressure," NASA/CR–2018–219737, published online Dec. 2018. https://ntrs.nasa.gov/citations/20180008699
45. Young, L. A., Chen, R. T. N., Aiken, E. W., Briggs, G. A., "Design Opportunities and Challenges in the Development of Vertical Lift Planetary Aerial Vehicles," Proceedings of the American Helicopter Society International Vertical Lift Aircraft Design Specialist's Meeting, January 2000.
46. Young, L. A., "Vertical Lift - Not Just for Terrestrial Flight," Proceedings of the AHS/AIAA/RaeS/SAE International Powered Lift Conference, Arlington, VA, October 30- November 1, 2000.
47. Lorenz, R. D., "Post-Cassini exploration of Titan: Science rationale and mission concepts," Journal British Interplanetary Society, Vol. 53 No. 7/8, 2000, pp. 218-234.
48. Lorenz, R. D., "Flexibility for Titan Exploration: The Titan Helicopter," Forum on Innovative Approaches to Outer Planetary Exploration 2001–2020, Feb. 2001.
49. Young, L. A., "Exploration of Titan Using Vertical Lift Aerial Vehicles," Forum on Innovative Approaches to Outer Planetary Exploration 2001–2020, Feb. 2001.
50. Lorenz, R. D., "Flight power scaling of airplanes, airships, and helicopters: Application to planetary exploration," Journal of Aircraft, Vol. 38 No. 2, pp 208-214, 2001. https://doi.org/10.2514/2.2769
51. Young, L.A., "Exploration of Titan Using Vertical Lift Aerial Vehicles," NASA Headquarters and Lunar and Planetary Institute Forum on Innovative Approaches to Outer Planetary Exploration, LPI Contribution # 1084, Houston, TX, February 21-22, 2001.
52. Barnes, J., Lemke, L., Foch, R., McKay, C., Beyer, R., Radebaugh, J., Atkinson, D., Lorenz, R., Le Mouelic, S., Rodriguez, S., Bain, S., Kattenhorn, S., Colaprete, A., "AVIATR – Aerial Vehicle for In-Situ and Airborne Titan Reconnaissance," Experimental Astronomy, Vol. 33 No. 1, pp. 55–127 (2012). https://doi.org/10.1007/s10686-011-9275-9
53. Stofan, E., Lorenz, R., Lunine, J., Bierhaus, E., Clark, B., Mahaffy, P., Ravine, M., "TiME—The Titan Mare Explorer," IEEE Aerospace Conference, Big Sky, MT, paper 2434, 2013.
54. Young, L., Pascal, L., Aiken, E., Briggs, G., Withrow–Maser, S., Pisanich, G., Cummings, H., "The Future of Rotorcraft and other Aerial Vehicles for Mars Exploration," Presented at the Vertical Flight Society's 77th Annual Forum & Technology Display, Virtual, May 10-14, 2021. https://rotorcraft.arc.nasa.gov/Publications/files/77-2021-0064_Young.pdf
55. Radotich, M., Withrow–Maser, S., deSouza, Z., Gelhar, S., Gallagher H., "A Study of Past, Present, and Future Mars Rotorcraft," Presented at the Vertical Flight Society's 9th Biennial Autonomous VTOL Technical Meeting, Virtual, January 26-28, 2021. https://rotorcraft.arc.nasa.gov/Publications/files/RadotichaVTOL_Tech_Meeting_Final_Revised_012521.pdf
56. Young, L., Deluane J., Johnson W., Withrow–Maser, S., Cummings, H., Sklyanskiy E., Izraelevitz J., Schutte, A., Fraeman, A., Bhagwat, R., T. "Design Considerations for

a Mars Highland Helicopter," Presented at the AIAA Ascend Conference, Virtual, November 16–18, 2020. https://rotorcraft.arc.nasa.gov/Publications/files/Mars_Highlands_Helicopter_AIAA_ASCEND_Final.pdf
57. Withrow–Maser, S., Johnson W., Young L., Koning, W., Kuang, W., Malpica C., Balaram J., Tzanetos, T., "Mars Science Helicopter: Conceptual Design of the Next Generation of Mars Rotorcraft," Presented at the AIAA Ascend Conference, Virtual, November 16–18, 2020. https://rotorcraft.arc.nasa.gov/Publications/files/MSH_summary_AIAA_ASCEND_final.pdf
58. Withrow-Maser, S., Koning W., Kuang W., Johnson, W., "Recent Efforts Enabling Future Mars Rotorcraft Missions," Presented at the VFS Aeromechanics for Advanced Vertical Flight Technical Meeting, San Jose, CA, January 21–23, 2020. https://rotorcraft.arc.nasa.gov/Publications/files/Shannah_Withrow_TVF_2020.pdf
59. Johnson, W., Withrow-Maser, S., Young, L., Malpica, C., Koning, W.J.F., Kuang, W., Fehler, M., Tuano, A., Chan, A., Datta, A., Chi, C., Lumba, R., Escobar, D., Balaram, J., Tzanetos, T., Grip, H., "Mars Science Helicopter Conceptual Design," NASA/TM–2020–220485. https://rotorcraft.arc.nasa.gov/Publications/files/MSH_WJohnson_TM2020rev.pdf
60. Cornelius, J., Schmitz, S., Palacios, J., Passe, B., Heisler, R., "Verification of RotCFD for Coaxial Rotor Performance," under review in AIAA Journal of Aircraft.
61. KDE Direct, KDE-CF305 Design Geometry Dimensions Specification Sheet, Bend, OR, 2021. https://www.kdedirect.com/
62. ATI Industrial Automation Inc., F/T Sensor: Delta Calibration, Apex, NC, 2021. https://www.ati-ia.com/products/ft/ft_models.aspx?id=delta
63. Cornelius, J., Kinzel, M., and Schmitz, S., "Efficient Computational Fluid Dynamics Approach for Coaxial Rotor Simulations in Hover," *AIAA Journal of Aircraft*, Vol. 58, No. 1, January-February 2021. https://doi.org/10.2514/1.C036037
64. Sukra Helitek, RotCFD: Rotor Computational Fluid Dynamics Integrated Design Environment, Software Package, Ver. 0.9.15 Build 402, Ames, IA, 2020. http://sukra-helitek.com/
65. Rajagopalan, G., Baskaran, V., Hollingsworth, A., Lestari, A., Garrick, D., Solis, E., and Hagerty, B., "RotCFD – A Tool for Aerodynamic Interference of Rotors: Validation and Capabilities," AHS Future Vertical Lift Aircraft Design Conference, San Francisco CA, Jan. 2012. https://rotorcraft.arc.nasa.gov/Publications/files/A-5-D_rajagopalan.pdf
66. Schatzman, N., "Aerodynamics and Aeroacoustic Sources of a Coaxial Rotor," NASA/TM-2018-219895, Nov. 2018. https://ntrs.nasa.gov/citations/20180003216
67. Conley S, Russell C, Kallstrom K, Koning W, Romander E., "Comparing RotCFD Predictions of the Multirotor Test Bed with Experimental Results," VFS Forum 76, Oct. 2020.
68. Rajagopalan, G., Thistle, J., and Polzin, W., "The Potential of GPU Computing for Design in RotCFD," AHS Technical Meeting on Aeromechanics Design for Transformative Vertical Lift, San Francisco, CA, Jan. 2018. https://rotorcraft.arc.nasa.gov/Publications/files/Rajagopalan_2018_TechMx.pdf
69. Koning, W., Johnson, W., and Grip, H., "Improved Mars Helicopter Aerodynamic Rotor Model for Comprehensive Analyses," AIAA Journal, Vol. 57, No. 9, Sept. 2019. https://doi.org/10.2514/1.J058045
70. Koning, W., "Generation of Performance Model for the Aeolian Wind Tunnel (AWT) Rotor at Reduced Pressure," NASA/CR–2018–219737, published online Dec. 2018. https://ntrs.nasa.gov/citations/20180008699
71. C81 Airfoil Table Generator using ARC2D (Efficient Two-Dimensional Solution Methods for the Navier-Stokes Equations), Software Package, Build: July 2018, Ames, IA. http://sukra-helitek.com/
72. Drela, M., "XFOIL: An Analysis and Design System for Low Reynolds Number Airfoils," Low Reynolds Number Aerodynamics, Springer, Berlin, Heidelberg, 1989, pp 1-12. https://web.mit.edu/drela/Public/web/xfoil/
73. Critzos, C., Heyson, H., and Boswinkle, R., "Aerodynamic Characteristics of NACA 0012 Airfoil Section at Angles of Attack From 0-180 Degrees," NACA TN-3361, Jan. 1955. https://ntrs.nasa.gov/citations/19930084501
74. Viterna, L., and Corrigan, R., "Fixed Pitch Rotor Performance of Large Horizontal Axis Wind Turbines," DOE/NASA Workshop on Large Horizontal Axis Wind Turbines, published online Jan. 1982. https://ntrs.nasa.gov/citations/19830010962
75. Tangler, J., and Kocurek, D., "Wind Turbine Post-Stall Airfoil Performance Characteristics Guidelines for Blade-Element Momentum Methods," 43rd AIAA Aerospace Sciences Meeting and Exhibit, AIAA-2005-591, Reno, NV, 2005. https://doi.org/10.2514/6.2005-591